Available online at www.sciencedirect.com
ScienceDirect
Journal of Power Sources 180 (2008) 243–252
JOURNAL OF POWER SOURCES
www.elsevier.com/locate/jpowsour

Sequential flow membraneless microfluidic fuel cell with porous electrodes

Kamil S. Salloum [a], Joel R. Hayes [b], Cody A. Friesen [b], Jonathan D. Posner [a,*]

[a] *Department of Mechanical and Aerospace Engineering, Arizona State University, Tempe, AZ 85287-6106, United States*
[b] *School of Materials, Arizona State University, Tempe, AZ 85287-8706, United States*

Received 17 November 2007; received in revised form 29 December 2007; accepted 31 December 2007
Available online 17 January 2008

Abstract

A novel convective flow membraneless microfluidic fuel cell with porous disk electrodes is described. In this fuel cell design, the fuel flows radially outward through a thin disk shaped anode and across a gap to a ring shaped cathode. An oxidant is introduced into the gap between anode and cathode and advects radially outward to the cathode. This fuel cell differs from previous membraneless designs in that the fuel and the oxidant flow in series, rather than in parallel, enabling independent control over the fuel and oxidant flow rate and the electrode areas. The cell uses formic acid as a fuel and potassium permanganate as the oxidant, both contained in a sulfuric acid electrolyte. The flow velocity field is examined using microscale particle image velocimetry and shown to be nearly axisymmetric and steady. The results show that increasing the electrolyte concentration reduces the cell Ohmic resistance, resulting in larger maximum currents and peak power densities. Increasing the flow rate delays the onset of mass transport and reduces Ohmic losses resulting in larger maximum currents and peak power densities. An average open circuit potential of 1.2 V is obtained with maximum current and power densities of 5.35 mA cm^{-2} and 2.8 mW cm^{-2}, respectively (cell electrode area of 4.3 cm^2). At a flow rate of 100 μL min^{-1} a fuel utilization of 58% is obtained.
© 2008 Elsevier B.V. All rights reserved.

Keywords: Laminar flow fuel cell; Sequential flow; Membraneless fuel cell; Porous electrode; Formic acid fuel cell; Microfluidic fuel cell

1. Introduction

Small scale and microfluidic fuel cells have gained much interest over the past few years as power sources for portable electronic devices [1]. Many microfabricated fuel cells use membrane-based architectures which are essentially small versions of full scale fuel cell systems [2–9]. Both full scale and miniature fuel cells that use PEM membranes have significant technical challenges including water management [7,10,11], membrane degradation [12–16], and crossover of liquid reactants [17–22]. Some small-scale microfluidic fuel cells use flowing liquid electrolytes as a replacement for polymer electrolyte membranes (PEM) [23,24]. These membraneless fuel cells alleviate membrane degradation issues, offer greater flexibility with fuel and oxidant selection, and can operate in acidic or basic media. Liquid reactants are preferable from fuel safety, storage, and energy density standpoints [25]. However, membraneless fuel cells typically exhibit higher Ohmic losses which result in lower power densities than membrane-based fuel cells. In addition, a liquid background electrolyte results in increased weight, thus reducing the overall gravimetric power and energy density. Membraneless fuel cells have been demonstrated with vanadium(II/IV) [26,27], formic acid [23], and hydrogen saturated acids [28] as fuels and potassium permanganate, hydrogen peroxide, and oxygen saturated acids as oxidants including oxygen in air with a cathode gas diffusion layer [24].

In low Reynolds number regimes, co-flowing parallel streams of liquid fuel and oxidant develop a laminar interface which acts as a virtual membrane [23,26]. The convecting laminar flow interface allows for the migration of cations (usually protons), transverse to the flow direction from the anode to the cathode. The catalyst is typically located along the entire length of the microchannel sidewalls. Parallel flow cell designs require careful consideration of the development of both the viscous and concentration boundary layers. In parallel flow designs the flow rates are linked to the power density and fuel utilization. The power density of parallel flow fuel cells increases with increasing flow rate. Higher flow rates generate higher power because they reduce the concentration boundary layer thickness at the

* Corresponding author. Tel.: +1 480 965 1799; fax: +1 480 965 1384.
E-mail addresses: jposner@asu.edu, jonathan.posner@asu.edu (J.D. Posner).

0378-7753/$ – see front matter © 2008 Elsevier B.V. All rights reserved.
doi:10.1016/j.jpowsour.2007.12.116

Table 1
Characteristics and performance summary of formic acid fuel cells

Type	Peak power density	Area (cm^2)	OCP (V)	Formic acid	Oxidant	Reference
Membraneless	2.5 mW cm^{-2} at 4 mA cm^{-2}	0.3	1.15	2 M	144 mM $KMnO_4$	Choban et al. [23]
Membraneless	26 mW cm^{-2} at 100 mA cm^{-2}	0.3	0.95	1 M	Air	Jayashree et al. [24]
Membraneless	0.7 mW cm^{-2} at 0.75 mA cm^{-2}	0.02	1.0	2 M	144 mM $KMnO_4$	Sun et al. [30]
Membraneless	0.18 mW cm^{-2} at 0.65 mA cm^{-2}	0.5	0.64	0.5 M	Air in 0.1 M H_2SO_4	Cohen et al. [29]
PEM	34 mW cm^{-2} at 200 mA cm^{-2}	1	0.75	6 M	Air	Ha et al. [8]
PEM	177 mW cm^{-2} at 334 mA cm^{-2}	4	0.9	12 M	Air	Ha et al. [2]
PEM	50 mW cm^{-2} at 130 mA cm^{-2}	5	0.72	9 M, 60 °C	Humidified O_2, 70 °C	Rice et al. [4]
PEM	16 mW cm^{-2} at 70 mA cm^{-2}	0.44	0.6	10 M	O_2	Yeom et al. [7]
PEM	160 mW cm^{-2}at 600 mA cm^{-2}	5	0.7	3 M, 60 °C	Air, 60 °C	Zhu et al. [5]

electrodes resulting in lower mass transport losses. The improvements in power density come at the expense of fuel utilization because the fuel and oxidant reach the end of the cell before they are consumed. Since the flow rate and the mass transport at the electrode are tightly coupled, efforts have been made to alter the microchannel geometry to improve the mass transport behavior and cell performance. For example, Kjeang et al. [27] increased electrocatalyst surface area using stacks of graphite rods in a vanadium-redox fuel cell in an effort to improve efficiency, Cohen et al. [29] introduced a planar tapered flow that delays the onset of reactant depletion to increase utilization, and Sun et al. [30] introduced a parallel flowing electrolyte between the reactant streams in order to reduce reactant mixing.

In parallel flow designs, unreacted fuel and oxidant mix by diffusion at the laminar flow interface which results in a decrease in the maximum possible fuel utilization. Mixing of the fuel and oxidant decreases with increasing flow rate because the reactants are advected downstream with greater velocity (greater Peclet number) [31]. Although larger flow rates should result in less mixing of the streams at the interface, the fuel and oxidant may reach the end of the cell before they are consumed, resulting in a net reduction in fuel utilization.

Table 1 displays a summary of recent work on formic acid fuel cells. In general, PEM-based formic acid fuel cells provide higher current densities and peak power values relative to membraneless fuel cells due to the higher concentration of formic acid used and their lower Ohmic resistances. We attribute the lower Ohmic losses to higher conductance of polymer membranes over liquid membraneless fuel cells. The conductance of membraneless formic acid fuel cells depends on the protic conductivity of the reactants and supporting electrolyte as well as the area and length of the conducting zone. On the other hand, membraneless fuel cells exhibit higher open circuit potentials since fuel crossover to the cathode is reduced when proper flow rate conditions and cell designs are used.

In this work we present a novel membraneless fuel cell where the fuel and oxidant flow in series. Fig. 1 shows a schematic of the sequential flow membraneless fuel cell with porous disk electrodes. The fuel stream is introduced at the center of the anode and flows radially outwards through a porous disk electrode with diameter D_a and height h. As the fuel flows radially outward, it is oxidized on Pt nanoparticles coating the surface of the porous electrode. Electrons are conducted through an external circuit and react with the oxidant at the cathode. Ideally, all the fuel is completely oxidized before exiting the anode which may alleviate issues related to mixing of unreacted fuel and oxidant. The oxidant is introduced in series with the fuel, at a location radially outward from the anode, approximately $r = D_a/2 + g$. The oxidant and oxidized fuel combine and flow towards an annular disk porous cathode with width $D_{c2} - D_{c1}$ and height h. The oxidant is reduced at the cathode, complexes with the

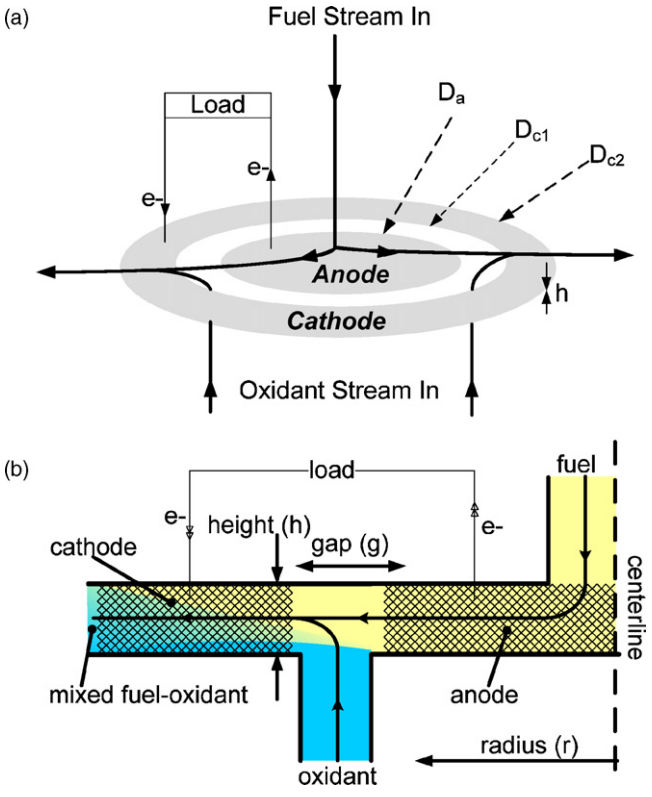

Fig. 1. Schematics of electrode design and flow paths of the radial membraneless fuel cell as (a) isometric projection and (b) cross-section of the radial flow fuel cell. The fuel stream is introduced to the center of the anode disc, and flows radially outward as it undergoes oxidation. The oxidized species flows through a membraneless gap, where it mixes with the oxidant stream just prior to flowing through the cathode. The reaction is then completed within the cathode. Electrons are routed through an external circuit through platinum wires in contact with the electrode surfaces. The electrode dimensions are 10.2 mm (D_a), 14.0 mm (D_{c1}), 25.4 mm (D_{c2}), and 0.1 mm (h) and $g = 2$ mm.

oxidized fuel, and continues to flow outward away from the cathode towards an azimuthally distributed waste outlet. The oxidant stream should not reach the anode so to avoid mixed potentials. The gap between the anode and cathode serves as an electronic insulator between the anode and cathode as well as separates the fuel and oxidant under the defined flow field. The oxidant will not reach the anode as long as the flows are laminar and stable, and the radial convective velocity at the interface between the two streams is greater than the characteristic speed of diffusion of the oxidant (as described in Section 4).

This sequential flow configuration improves mass transport by advecting the reactants through porous electrodes and advecting waste products downstream. In addition, the streams are not advected in parallel thereby avoiding a diffuse interface along the length of the cell. Using the current cell design, it may be possible to completely oxidize the fuel and reduce the oxidant so that the two reactants will not mix and result in mixed potentials and poor fuel utilization. This fuel cell architecture allows for tuning of the electrode surface areas as well as the independent control of the fuel and oxidant flow rates. This paper presents a radial flow fuel cell that is constructed of bulk machined polymethyl methacrylate (PMMA), carbon paper electrodes, and Pt black catalyst. The fuel used is formic acid in sulfuric acid. The oxidant is potassium permanganate in sulfuric acid. Using particle image velocimetry, we show that the fluid flow field in the fuel cell is radially outward and axisymmetric. We characterize cell performance as a function of the fuel and oxidant flow rate as well as the electrolyte concentration.

In Section 2 we discuss the cell construction, chemistry, and experimental set-up used; in Section 3 we present the flow velocimetry results, cell potential and power characterization, as well as the calculated cell resistance and fuel utilization; and in Section 4 we discuss our results relative to existing membraneless fuel cells.

2. Experimental methods

2.1. Cell construction

In this section we describe the dimensions, materials, and construction of the fuel cell and electrodes. The experimental apparatus is reported along with the fuel cell chemistry and the experimental conditions tested.

Fig. 2 represents a scaled solid model of the radial fuel cell housing. The cell consists of a top and bottom milled PMMA plate, sandwiched by machined 316 stainless steel disks. The steel disks have a radial bolt-hole pattern that acts as a super structure to maintain conformal contact over the entire cell surface. A mixture of formic acid and sulfuric acid (throughout called the fuel) flows through a 1.58 mm hole drilled in the 6.35 mm thick top plate. The fuel is oxidized as it flows through the anode, across the gap and into the cathode. A mixture of potassium permanganate and sulfuric acid (oxidant) is introduced concentrically through a ring of inlets in the approximately 2 mm wide gap and mixes with the oxidized fuel as it flows to the cathode. The waste products are routed out of the cell through concentric outlets placed at $r = 18.5$ mm. A third PMMA plate distributes the waste products. PEEK liquid chromatography ports (N-333, Upchurch Scientific, Oak Harbor, WA) were used to deliver liquid reactants to the fuel cell. The ports were bonded to the PMMA structures by curing the supplied adhesive rings at 92 °C for 15 h. Fluorosilicone flat polymer rings with an uncompressed thickness of 400 μm were cut using a laser ablation system (Universal Laser Systems, Scottsdale, AZ) and served as support for the concentric catalyst structures.

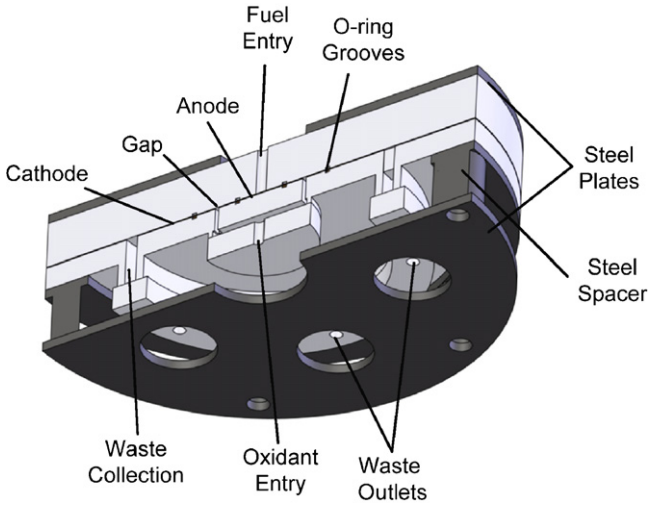

Fig. 2. Scaled cross-section of assembled radial flow fuel cell. The darker structures are constructed of stainless steel, the light colored structures are made from acrylic (PMMA). The cell was fabricated on a 3-axis CNC mill.

The electrodes are fabricated from Toray carbon paper (E-TEK, Somerset, NJ) and platinum black (HiSPEC^{TM} 1000, Alfa Aesar, Ward Hill, MA). The anode is 5.1 mm in radius and approximately 100 μm thick. The cathode annulus has an inner radius of 7.0 mm and an outer radius of 12.7 mm. Fig. 1a shows the electrode shapes with anode and cathode projected surface areas of 0.8 and 3.5 cm^2, respectively. Electrocatalysts were prepared by mixing 5 mg Pt black in isopropyl alcohol (CAS 67-63-0, Fisher Scientific, Waltham, MA) and depositing onto the Toray paper (as described in [25]). The Pt coated paper was placed under vacuum overnight to remove residual alcohol. Current was collected with a 0.127 mm platinum wire placed in contact with the electrode and sandwiched by the gaskets.

The reactants were delivered to the fuel cell by two independent programmable syringe pumps (KDS200, KD Scientific, Holliston, MA). The fuel cell leads were connected to a source meter (Model 2410, Keithley Instruments, Cleveland, OH) operating in galvanostatic mode. Galvanostatic measurements were taken in steps of 0.2 or 0.5 mA, starting from open circuit potential. The current and voltage were collected using a PC and Labview (National Instruments, Austin, TX) connected to the source meter via GPIB interface. After each change in the current, the cell requires 10–15 s to reach a steady state voltage. The voltages reported here are time averaged over 30 s after the transient response.

For the flow characterization experiments, we use microscale particle image velocimetry (μPIV) to track the flow velocity in the cell. μPIV infers the fluid flow velocity by tracking the displacement of particle flow tracers over two instantaneous images

[32]. The flow tracers used are 5 μm fluorescent polystyrene microspheres (G0500, Duke Scientific, Fremont, CA) diluted in DI water. The particle motion is imaged using an inverted epifluorescence microscope (TE2000U, Nikon, Tokyo, Japan), 1×, 0.10 NA objective, and a cooled 16-bit CCD camera (Cascade 512IIB, Roper Scientific, Tucson, AZ). The low numerical aperture objective results in fluid measurements that are depth averaged across the height of the cell. Captured flow images were cross-correlated and validated using PIV Sleuth (Laboratory for Turbulent and Complex Flow, UIUC). The time between exposures was 168.5 ms with an average particle displacement of 10 pixels. The cross-correlations were calculated using interrogation windows of 32×32 pixels and 50% overlap. The displacements are determined using a 9-point-based Gaussian interpolation of the correlation maps. The fluid velocity vector fields reported are validated using an 8 neighbor magnitude comparison and an average of 10 image pairs.

2.2. Chemistry

Reactants were prepared by dilution in the supporting electrolyte of 0.5 or 1 M sulfuric acid (CAS 7664-93-9, EMD Chemicals, Hibbstown, NJ) in 18.3 MΩ deionized water (Millipore, Billerica, MA). The fuel and oxidant are formic acid (CAS 64-18-6, Sigma–Aldrich, St. Louis, MO) and potassium permanganate (CAS 7722-64-7, Sigma–Aldrich, St. Louis, MO), respectively. The electrochemical reaction at the anode is [33]:

$$\mathrm{HCOOH} \leftrightarrow \mathrm{CO_2} + 2\mathrm{H^+} + 2\mathrm{e^-} \quad (E^\circ = -0.199\,\mathrm{V\ vs.\ SHE}) \tag{1}$$

The anodic reaction involves the production of carbon dioxide. Carbon dioxide is soluble in aqueous solvents, at standard room temperature and pressure, up to a mole fraction of approximately 6×10^{-4} [33], equivalent to 33 mM. At the largest currents tested (23 mA), the CO_2 generation rate is 1.2×10^{-7} mol s^{-1}. At a flow rate of 5000 μL min^{-1} we expect a dissolved CO_2 molarity of 1.44 mM. This molarity is well within the solubility limits of CO_2 gas in aqueous solutions. Therefore, there is no carbon dioxide bubble nucleation in the solution.

Although there are various routes for permanganate reduction, the primary permanganate reduction at the cathode is in an acidic medium and is given by

$$\mathrm{MnO_4^-} + 8\mathrm{H^+} + 5\mathrm{e^-} \leftrightarrow \mathrm{Mn^{2+}} + 4\mathrm{H_2O} \quad (E^\circ = 1.507\,\mathrm{V\ vs.\ SHE}) \tag{2}$$

In the presence of the permanganate ion, Mn(II) is oxidized in acid media and produces the insoluble MnO_2 through the reaction [34]:

$$2\mathrm{MnO_4^-} + 3\mathrm{Mn^{2+}} + 2\mathrm{H_2O} \leftrightarrow 5\mathrm{MnO_{2(s)}} + 4\mathrm{H^+} \quad (E^\circ = 0.46\,\mathrm{V\ vs.\ SHE}) \tag{3}$$

The maximum theoretical open circuit potential is predicted as 1.706 V, assuming all reactants are completely oxidized or reduced, but this may be lowered by the secondary reaction given in (3).

Table 2
Summary of experimental conditions

Parameter	Range
Flow rate	100–5000 μL min^{-1}
Supporting electrolyte concentration	0.5/1 M
Oxidant concentration	1–100 mM
Fuel concentration	3–40 mM
Fuel:oxidant flow rate ratio	1/2

We investigated a variety of experimental conditions, including: the supporting electrolyte concentration; the oxidant and fuel flow rates; and the fuel–oxidant flow rate ratio. Table 2 shows a summary of the experimental parameters. The permanganate concentration was fixed at 10 mM because at higher concentrations MnO_2 precipitates (see Eq. (3)) and settles in the pores of the cathode carbon paper occluding fluid flow in the cell. The formic acid concentration was fixed at 40 mM to remain within the stoichiometric range of the net reaction. The maximum flow rate was 5 mL min^{-1}, as the cell leaks at higher flow rates due to the pressure required to sustain the flow. The sulfuric acid concentration was investigated at 0.5 and 1 M.

3. Results and analysis

Here we present the results and analysis of the flow field measurements and electrochemical characterization of the radial flow fuel cell. Fuel cell polarization curves, power density, resistance, and fuel utilization are reported as a function of the flow rates and electrolyte concentration.

3.1. Characterization of the flow field

The architecture of the radial flow fuel cell requires that the reactants flow uniformly towards the cathode. It is especially critical that the oxidant stream not reach the anode or mixed electrochemical potentials may be observed. We quantitatively measure the fluid velocity in the cell using μPIV. For these flow measurements, a 2.5 mm radius anode (smaller than that of the active cell) was used to increase the visible area in the gap. The vector field for fuel and oxidant flow rates of 500 μL min^{-1} is presented in Fig. 3a. Qualitatively, the vector field reveals a velocity distribution that spans radially out towards the cathode. The vector field is relatively symmetric in the azimuthal direction, with preferential fluid drift to the left side of the cell in the figure. We attribute the drift to the left side to reduced fluidic resistance due to larger height which is controlled by compression of the o-rings and carbon paper by the bolted super structure.

Since it is difficult to determine the height of the cell when fully constructed, we can estimate the effective height from the velocity field. Using mass conservation we can infer the effective hydraulic height of the cell using the depth averaged velocity measurement. The effective height is expressed as $h = Q/2\pi r V(r)$, where Q is the supplied flow rate of the fuel,

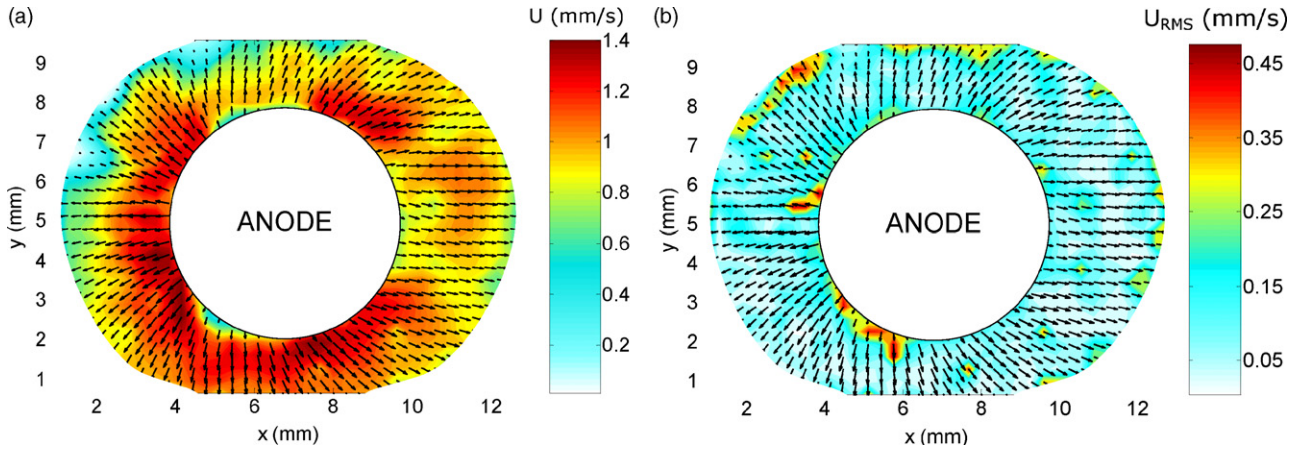

Fig. 3. (a) Average velocity field (10 image pairs) vectors in the radial flow fuel cell as measured using microscale particle image velocimetry. The contours show the average velocity magnitude. The field was obtained using epifluorescence microscopy of 5 μm diameter polystyrene spheres in the fuel stream with a flow rate of 500 μL min^{-1}. The anode for these measurements is 5 mm in diameter to allow visual access. (b) Countour map of velocity root mean square (RMS) map overlaid with average vectors. The RMS maps show a fairly steady flow field with variations to the left side of the anode. Visualization is truncated from the top and bottom due to limitations in region of interest.

r is the radial location of the measured velocity, and $V(r)$ is the flow velocity at r. Extracting a sample velocity of 1.0 mm s^{-1} at a radius of 4.0 mm from Fig. 3a (directly to the right of the anode), the effective height is calculated at 332 μm. Given that the Toray paper is approximately 100 μm thick, this implies that the gaskets were compressed from approximately 800 to 230 μm. A small effective height is desirable for the radial flow field as a smaller channel height provides viscous damping of the flow at the top and bottom walls similar to a Hele–Shaw flow [35]. The small height increases hydraulic resistance, thus isolating the flow between the electrodes from outside pressure perturbations.

Fig. 3b presents the calculated root mean square (RMS) map of the 10 velocity fields. The RMS velocity was calculated as [36]:

$$\boldsymbol{u}_{\mathrm{RMS}}(x, y) = \sqrt{\frac{\sum_{i=1}^{n}(\overline{\boldsymbol{U}}(x, y) - \boldsymbol{u}_i(x, y))^2}{n}} \quad (4)$$

where $\boldsymbol{u}(x, y)$ is the instantaneous velocity vector obtained from image pair i, $\bar{\boldsymbol{U}}$ is the average velocity vector across n image pairs, and quantities in bold are vectors. The computation was performed for both the x and y velocities over 10 image pairs, and the root of the sum of their squares was taken to produce the RMS map. The RMS map shows relatively low RMS values across the flow field, which indicates a steady flow. Toward the left side of the anode, regions of elevated RMS indicate some temporal flow variations. We inject 100 mM fluorescein (CAS 518-47-8, Fisher Scientific, Waltham, MA) into the cathode stream to visualize the path of the oxidant and the interface between the flow from fuel and oxidant. The cathodic stream does not perturb the anode flow enough to result in cathode fluorescein reaching the anode region. We obtain a steady interface between the cathodic and anodic flow with flow rate ratios (fuel:oxidant) as low as 0.5.

3.2. Fuel cell performance

Here we describe the variation of the fuel cell performance on the flow rate of the fuel and oxidant, the flow rate ratio, and the concentration of the supporting electrolyte. The reaction residence times, reaction product advection, and transport due to diffusion at the fuel/oxidant interface are all dependent on the flow rates of the fuel and oxidant. In addition, the supporting electrolyte is a critical parameter in governing Ohmic losses in the cell, as described later in Section 3.4.

Fig. 4 presents polarization (a) and power density (b) data for the radial membraneless fuel cell with various flow rates and supporting electrolyte concentrations. The flow rate ratios remain constant at 1:1. Here we report the current density and power density scaled by the fuel cell's total projected electrode area (4.3 cm^2). The area selection for this cell design is not straightforward and varies over a large range. For example, it is reasonable to choose the anode or cathode areas of 0.8 or 3.5 cm^2, respectively, or their sum. Alternatively the total area that the protons are transported through (~0.04 cm^2 at the edge of the anode) may be used. These areas vary by two orders of magnitude which may disguise the true performance of the cell. Alternatively, the volume of the cell (~6.5 cm^3) could be used, giving a volumetric power density which may be more appropriate for portable electronic applications. We chose total combined anode and cathode area for scaling of the current and power densities since it is the largest possible area.

In general the polarization curves show cell performance which is similar to other membrane [37] and membraneless [23] fuel cells. We observe an average open circuit potential of 1.2 V which is consistent with the values presented in Table 1. There is an initial decrease in the voltage due to polarization losses at the electrode surface followed by a region of nearly linear variation in the cell potential with current. The slope of the Ohmic region depends on both the concentration of the supporting electrolyte and the flow rate as discussed in Section 3.4. At higher current

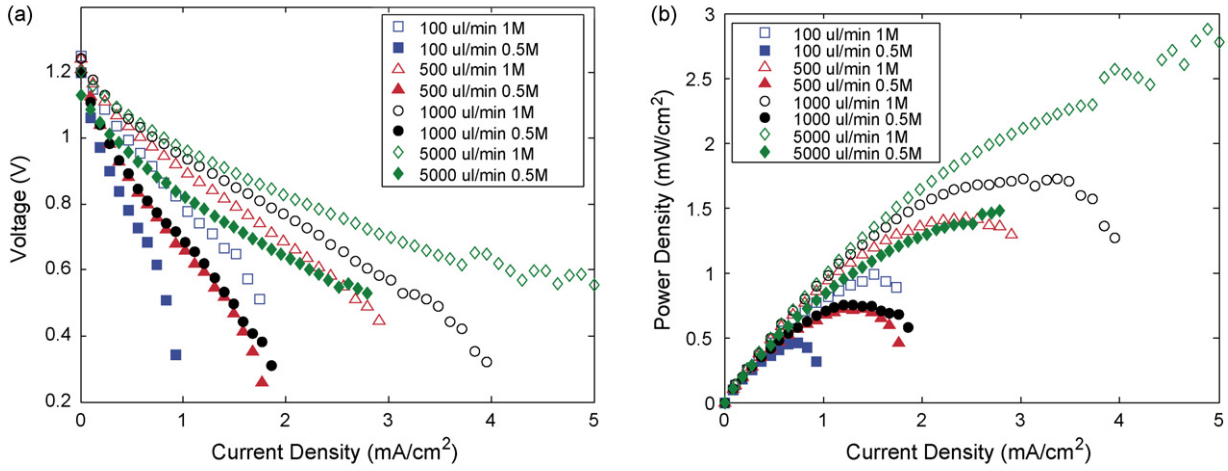

Fig. 4. Polarization (a) and power density (b) curves at various flow rates and electrolyte concentrations. The flow rate ratio of the fuel (40 mM formic acid) to the oxidant (10 mM potassium permanganate) is 1:1. Higher sulfuric acid concentration (as denoted in the legend) decreases the cell's internal resistance, thus increasing the potential at every current. Higher flow rates reduces the residence time of the reactants and thickness of the concentration boundary layer at the reaction surface, resulting in delay of mass transport losses to higher currents. The absolute current and power are normalized by the total electrode area of 4.3 cm^2.

densities and some operating conditions, we observe potential drops due to concentration polarization.

3.3. Dependence on flow rate

Fig. 4a shows that the cell potential increases with flow rate (1:1 ratio of fuel and oxidant) at a given current load. This trend has been observed in parallel flow membraneless fuel cells [27]. Higher flow rates not only reduce concentration boundary layer thicknesses, but also increase the turn over rate of the catalyst by removing adsorbed carbon monoxide due to the indirect oxidation (dehydration pathway) of formic acid [4]. At the cathode, we expect that higher flow rates will also reduce fouling from precipitated MnO_2. The maximum flow rate that was explored in the cell was 5 mL min^{-1}.

Fig. 5 shows the polarization (a) and power density (b) data for the cell at flow rate ratios of 1:1 and 2:1 (fuel:oxidant). It is apparent that a decrease in oxidant flow lowers the cell power. Both 1:1 and 2:1 ratios exhibit improved performance with flow rate. As the formic acid is oxidized, the potassium permanganate consumes protons from the background sulfuric acid based on the stoichiometry of the net reaction. However, when permanganate flow rate is decreased (analogous to a rich stoichiometry), the fuel oxidation is limited due to the decreased availability of oxidant at the cathode. As a result, unoxidized fuel flows out of the anode, reacts with the permanganate ions in the gap and further depletes the oxidant [38]. At 5 mL min^{-1} the performance of the cell is nearly identical at the two ratios, suggesting that the above limitations are overcome by the enhanced mass transport at the higher flow rates. Moreover, we observe a small increase in the open circuit potential of approximately 100 mV for the 1:1 flow rate ratio.

Fig. 6a shows the cell potential versus flow rate (1:1) for several imposed current loads. In general, the cell potential

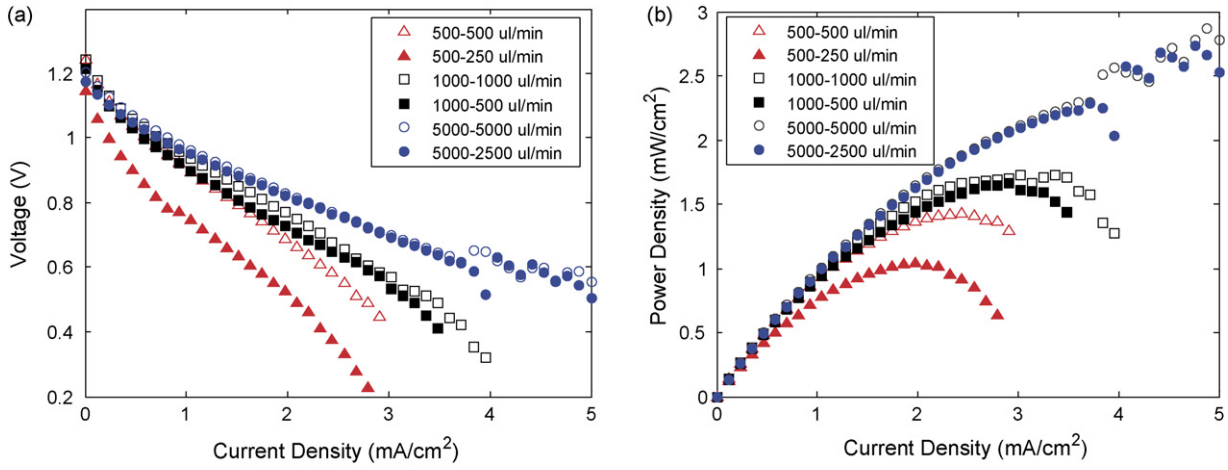

Fig. 5. Polarization (a) and power density (b) curves at 1:1 and 2:1 formic acid (40 mM) to potassium permanganate (10 mM) flow rates. The background sulfuric acid concentration was held constant at 1 M. Fuel rich conditions lower the potential of the cell (and hence power). We attribute the reduced potential to non-catalytic reaction of the unoxidized formic acid with the permanganate ions prior to cathode entry. The absolute current and power are normalized by the total electrode area of 4.3 cm^2.

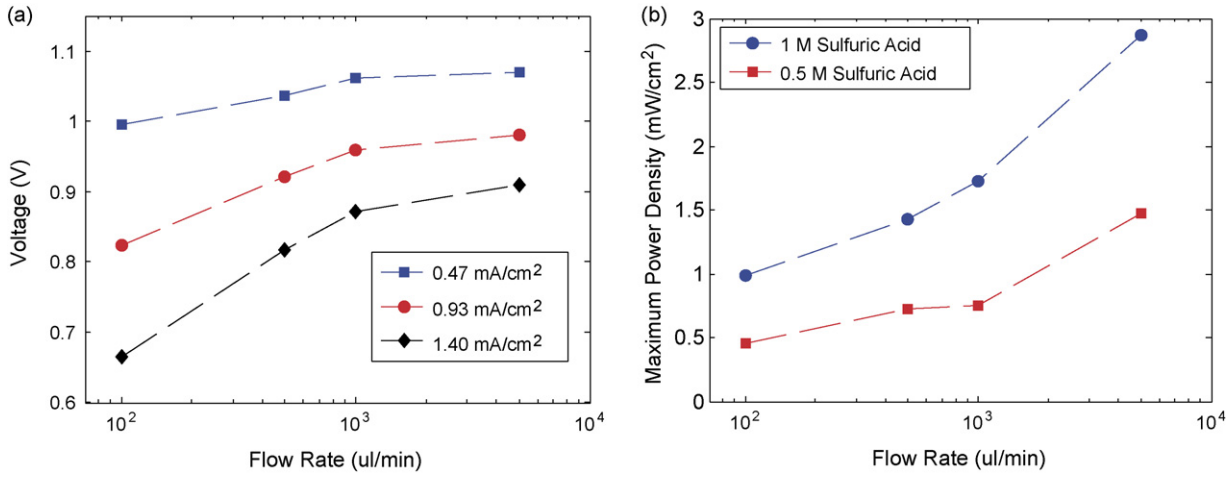

Fig. 6. (a) Cell potential vs. flow rate at different galvanostatic loads. The flow rate ratio is 1:1 for 40 mM formic acid and 10 mM potassium permanganate in 1 M sulfuric acid supporting electrolyte. (b) Maximum achieved power density vs. flow rate. The flow rate ratio is 1:1 for 40 mM formic acid and 10 mM potassium permanganate in sulfuric acid supporting electrolyte concentration denoted in the figure. The power density (normalized with the total 4.3 cm^2 electrode area) increases with flow rate due to reduction in Ohmic resistance and delay of mass transport losses.

increases with flow rate for a given load. At low flow rates <1000 $\mu L\,min^{-1}$, the potential increases steeply with flow rate. Note that this increase is more prominent at larger currents suggesting that mass transport losses are critical at higher loads. At larger flow rates, the potential is weakly dependent on the flow rate. We attribute this to improvements in mass transport and subsequent extension of the Ohmic loss regime. For example, Fig. 4a shows that at 100 $\mu L\,min^{-1}$ there are significant mass transport losses starting at 1.15 $mA\,cm^{-2}$. At flow rates in excess of 1000 $\mu L\,min^{-1}$, the polarization curves are linear at the same load and the mass transport losses are not apparent up to 2.8 $mA\,cm^{-2}$.

Fig. 6b shows the maximum fuel cell power as a function of the flow rate for two values of the supporting electrolyte concentration and a flow rate ratio of 1:1. We see that the power of the cell also increases with flow rate. Contrary to the cell potential, the maximum power has a weak dependence on the flow rate for low flow rates (<500 $\mu L\,min^{-1}$) and increases rapidly for higher flow rates. Again, this is due to improved mass transport in the electrodes and extension of the Ohmic regime to higher current densities. Although it appears that increasing the flow rate will continue to increase the cell power, the maximum flow rate is limited by the cell construction and will also result in poor fuel utilization as discussed in Section 3.5.

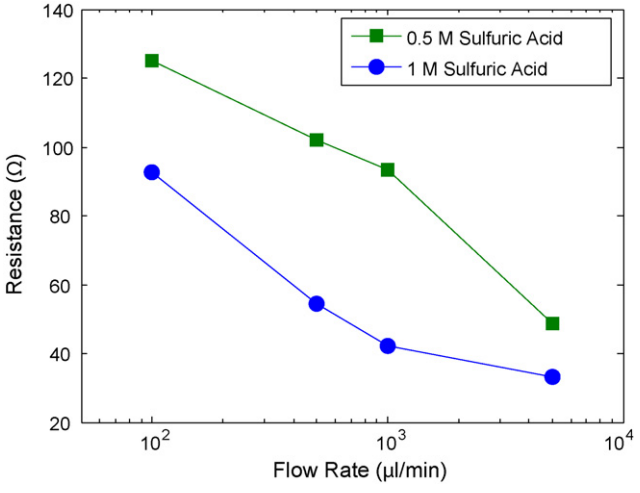

Fig. 7. Calculated Ohmic resistance vs. flow rate (ratio 1:1 fuel to oxidant). Supporting electrolyte concentrations are denoted in the legend. The Ohmic resistance is extracted from the linear region of the polarization curves shown in the figure.

3.4. Effect of supporting electrolyte concentration

In a membraneless fuel cell, the supporting electrolyte provides an electrochemical bridge from the anode to the cathode similar to the role of a semi-permeable membrane in a PEM fuel cell. The performance of the radial flow fuel cell is dependent on the ionic concentration of the supporting electrolyte. The Ohmic resistance of the cell is a critical factor in the cell performance. The total Ohmic resistance is a function of the individual resistive contributions of the electrodes, current collection leads, as well as the electrolyte in the gap. Fig. 4 demonstrates the effect of the electrolyte concentration. This figure shows that an increase of the sulfuric acid concentration from 0.5 to 1 M significantly lowers the Ohmic resistance of the cell. For example, the cell exhibits similar potentials at 5000 $\mu L\,min^{-1}$ at 0.5 M and 500 $\mu L\,min^{-1}$ with 1 M sulfuric acid. Increasing the supporting electrolyte concentration increases electrical potential and maximum power at each flow rate.

Fig. 7 presents a semi-log plot of the fuel cell's Ohmic resistance as a function of the flow rate, at both 0.5 and 1 M sulfuric acid concentrations. The resistance was calculated from the slope of the linear region of the polarization curves shown in Fig. 4a. Note that the resistance values here also reflect those of the current collection wires and leads, which were measured as approximately 4 Ω using a digital multimeter. The resistance of the electrolyte in the gap depends on the fuel cell and electrode geometry.

This data shows that doubling the sulfuric acid concentration reduces the Ohmic resistance of the cell (in some cases by half) which results in higher achievable currents, lower potential losses, and higher fuel cell power. An increase in sulfuric acid concentration yields higher solution conductivity across the anode to cathode gap, thus reducing Ohmic losses. The Ohmic losses reduce by nearly half when doubling the sulfuric acid concentration since the conductivity of the solution increases from 200 mS cm^{-1} at 0.5 M to 400 mS cm^{-1} at 1 M, measured using a conductivity meter. We expect the resistance to depend on the conductivity since the small gap between the anode and cathode provides an ionic bridge for the proton transfer. In the limit of small g, an approximation for the gap's resistance is $R = g/\sigma\pi h(D_a + g)$, where σ is the local conductivity of the solution in the gap. Based on the equation above, resistance is inversely proportional with σ and h, and varies nearly linear with the gap width g. Although larger values of h reduce the gap's electrical resistance, the laminar flow becomes more susceptible to perturbations as discussed in Section 3.1. Reducing the gap length should reduce the resistance and in this work is limited by manufacturing methods used and the ability to control the diffuse fuel and oxidant interface in the gap. We estimate the gap's electrical resistance to be approximately 3.3 Ω, based on the cell geometry and the solution conductivity of 1 M sulfuric acid.

Fig. 7 also shows that increasing the flow rate reduces Ohmic resistance of the cell. For example, at 0.5 M, an increase in the flow rate by 14 times reduces the Ohmic resistance by a factor of 2.6. This data suggests that there is a limit to the reduction of Ohmic losses by an increase of the flow rate. At 1 M supporting electrolyte, the resistance drops rapidly over the first decade of increasing flow rate, but appears to asymptote at higher flow rates. As is described in the next section, increasing the flow rate decreases the fuel utilization, and so flow rate can be used to tune the performance of the cell.

3.5. Fuel utilization

The fuel cell potential and power increases with flow rate, but results in lower fuel utilization. Assuming complete fuel dissociation (as shown in Eq. (1)), the fuel utilization is expressed as

$$\eta_i = \frac{I_i}{nFCQ_i} \tag{5}$$

where I is the measured current at a flow rate Q, n is the number of electrons transferred per mole (2 for formic acid), F is the Faraday's constant, and C is the concentration of formic acid (0.04 M). Fig. 8 shows a semi-log plot of η against the flow rate for 0.5 and 1 M sulfuric acid concentration. The utilization is calculated using the maximum measured current in the cell. The fuel utilization decreases with increasing flow rate from a maximum value of 0.58 at 100 μL min^{-1} to a minimum value of 0.04 at 5000 μL min^{-1} for the 1 M sulfuric acid, and from 0.31 at 100 μL min^{-1} to 0.02 at 5000 μL min^{-1} for the 0.5 M sulfuric acid. We attribute the decrease in the fuel utilization to the decrease in residence time for the formic acid oxidation.

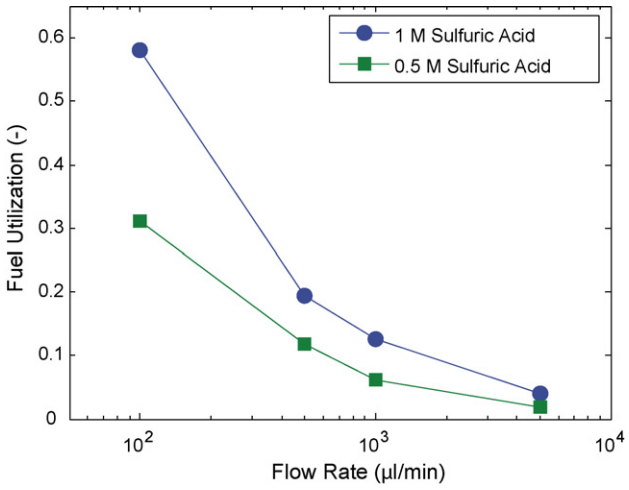

Fig. 8. Fuel utilization as a function of fuel (40 mM formic acid) and oxidant (10 mM potassium permanganate) flow rates with 1:1 ratio. Fuel utilization is calculated using maximum current. Supporting electrolyte concentrations are denoted in the legend. Although lower flow rates utilize fuel more efficiently, maximum power is compromised.

The current radial flow fuel cell exhibits the highest fuel utilization (58%) at a total power output of 4.1 mW to date, for a membraneless design running at a fuel flow rate of 100 μL min^{-1}. At the highest fuel flow rates of 5 mL min^{-1}, the fuel cell provided 12 mW at 4% fuel utilization (i.e. nearly factor of three increase in power at the expense of fuel utilization). Lower flow rates result in enhanced fuel utilization and higher energy density. Higher flow rates have greater power densities but lower utilization. It may be possible to increase the power at low flow rates without compromising utilization by increasing the concentration of the supporting electrolyte, increasing the surface area of the catalyst, or by using a fuel with greater electrochemical activity.

4. Discussion

Parallel flow membraneless fuel cells mitigate some of the challenges associated with PEM fuel cells by using a diffuse interface that is not ion-selective. The Peclet (Pe) number $Pe = UL/D$ defines the dominant transport processes in membraneless fuel cells, where U is the magnitude of the flow velocity, L is the characteristic length of diffusion, and D is the diffusion coefficient. At low Peclet numbers the dominant mode of transport is diffusive which mixes and depletes the reactants [23]. The diffusivity of formate, oxygen, and permanganate in an aqueous medium is approximately 1.5×10^{-5} cm^2 s^{-1}, 2.5×10^{-5} cm^2 s^{-1}, and 1.6×10^{-5} cm^2 s^{-1}, respectively [33]. Equivalent reactant diffusivities imply that species transport by diffusion is not a very efficient mechanism to prevent anions such as permanganate from diffusing into the fuel stream or reaching the anode, causing reactant depletion and mixed potentials. Increasing the Peclet number (i.e. by increasing the flow rate) results in less diffusive mixing at the expense of fuel utilization. At higher Peclet numbers the mass transport boundary layer is thinner which enhances mass

transport at the electrodes, but a greater fraction of the unreacted fuel is advected out of the cell and wasted.

Sequential flow fuel cells with porous electrocatalysts have distinct transport features. First, the porous electrodes have high surface area and narrow pores which reduce the length scales over which concentration gradients exist, reducing concentration polarization and improving fuel utilization. Second, the sequential flow pattern enables independent control of reactant flow rates and eliminates the linear diffuse interface responsible for reactant mixing and crossover. On the other hand, sequential flow results in mixing and crossover of fuel into the cathode if the fuel is not completely oxidized while passing through the anode. This requires careful tuning of the flow rates, electrocatalyst surface area, reactant concentrations, and current load. In addition, the radial design allows for independent variation of the projected electrode anode and cathode surface areas.

The sequential flow fuel cell exhibits polarization and power curves similar to both experimental and computational studies of parallel flow membraneless fuel cells. Our data reveals that increasing reactant flow rate delays the onset of mass transport losses and extends the Ohmic regime resulting in higher peak power densities in agreement with previous studies [27,28,30,39–41]. Ohmic resistance also decreases with flow rate as was shown by Kjeang et al. The perceived decrease in Ohmic resistance in membraneless fuel cells may actually be a reduction in mass transport losses. Moreover, fuel utilization decreases with flow rate (or *Pe* numbers) as observed in parallel flow cells [23,27] but the sequential cell attains higher fuel utilization than parallel flow designs because of the improved mass transport through the porous electrocatalysts. Fig. 8 shows that the fuel utilization (η) is approximately twice as large for 1 M sulfuric acid as for 0.5 M and that η asymptotes at large flow rates for both cases. Utilization increases with ionic strength at low flow rates because the maximum current at low flow rates is dictated by the Ohmic resistance. The Ohmic resistance decreases with concentration which yields larger maximum current as shown in Fig. 4. The utilization asymptotes at higher flow rates because in this regime the maximum current is controlled by mass transport.

Fig. 9 presents a summary of the fuel cell performance. The peak power density is plotted against its respective current density, at each investigated electrolyte concentration and reactant flow rate. The slope of this plot is the voltage at which the peak power is observed which is approximately 0.55 V. Higher maximum power potentials are attractive for small-scale fuel cells because DC voltage multiplication is more efficient at higher voltages and smaller numbers of cells in series are required to reach the desired voltage. The data also presents a correlation between the electrolyte concentration and flow rate. For example, the power density at a flow rate of 100 μL min^{-1} and electrolyte concentration of 1 M is approximate to that of a flow rate of 1000 μL min^{-1} and electrolyte concentration of 0.5 M. This suggests that from an energy density standpoint, it is more attractive to have a higher electrolyte concentration because less volume and weight of reactants are required to produce the same power. Fig. 9 can be used as a design curve for predicting fuel cell performance for specific power and current needs.

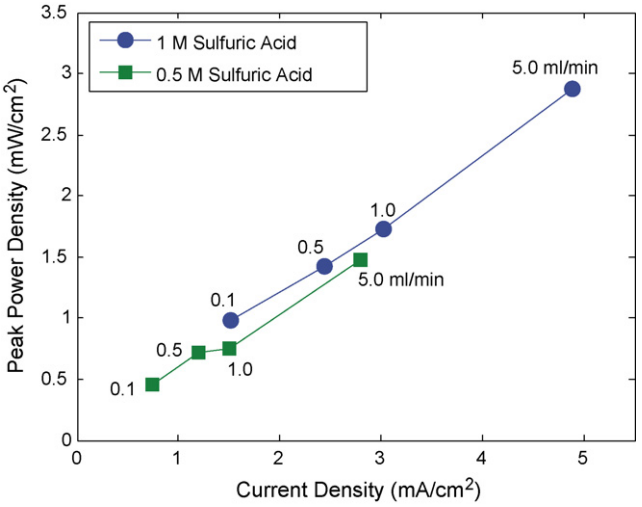

Fig. 9. Peak power density as a function of current density, electrolyte concentration, and flow rate (1:1 flow ratio of 40 mM formic acid and 10 mM potassium permanganate). The slope of the line (~0.55 V) is the operating voltage at peak power.

5. Conclusions

We present a novel sequential convective flow membraneless microfluidic fuel cell with porous disk electrodes, and demonstrated its operation with formic acid as the fuel and potassium permanganate as the oxidant. This fuel cell architecture enables independent control over the fuel, oxidant flow rate, and the electrode areas. The cell is machined out of PMMA and uses carbon paper coated with Pt black as the porous electrodes. The flow field was quantified to be nearly axisymmetric and steady using microscale particle image velocimetry. Increasing the supporting electrolyte concentration reduces the cell Ohmic resistance, resulting in larger cell currents and maximum power. Increasing the flow rate delays the onset of mass transport losses to higher currents and reduces Ohmic losses, resulting in greater cell power density. Increasing the flow rate reduced the fuel utilization from 58% at 100 μL min^{-1} to 4% at 5 mL min^{-1}. This cell performs with higher fuel utilization at each reactant flow rate than other membraneless fuel cell designs due to improved mass transport in the porous electrocatalyst. The maximum respective current and power obtained were 23 mA and 12 mW (4.3 cm^2 active area).

Acknowledgments

The authors thank True North partners and the Ira A. Fulton Graduate Fellowship Program for financial support of this work. KS acknowledges the Ira A. Fulton School of Engineering Machine Shop at Arizona State University for fabrication of the fuel cell, and thanks Steven A. Klein and Michael J. Murphy for discussions on PIV image acquisition and analysis.

References

[1] J.D. Morse, Int. J. Energy Res. 31 (6/7) (2007) 576–602.
[2] S. Ha, Z. Dunbar, R.I. Masel, J. Power Sources 158 (1) (2006) 129–136.

[3] Y.Q. Jiang, X.H. Wang, L.Y. Zhong, L.T. Liu, J. Micromech. Microeng. 16 (9) (2006) S233–S239.
[4] C. Rice, R.I. Ha, R.I. Masel, P. Waszczuk, A. Wieckowski, T. Barnard, J. Power Sources 111 (1) (2002) 83–89.
[5] Y.M. Zhu, S.Y. Ha, R.I. Masel, J. Power Sources 130 (1/2) (2004) 8–14.
[6] S.C. Yao, X.D. Tang, C.C. Hsieh, Y. Alyousef, M. Vladimer, G.K. Fedder, C.H. Amon, Energy 31 (5) (2006) 636–649.
[7] J. Yeom, G.Z. Mozsgai, B.R. Flachsbart, E.R. Choban, A. Asthana, M.A. Shannon, R. Kenis, Sens. Actuators B: Chem. 107 (2) (2005) 882–891.
[8] S. Ha, B. Adams, R.I. Masel, J. Power Sources 128 (2) (2004) 119–124.
[9] S. Aravamudhan, A.R.A. Rahman, S. Bhansali, Sens. Actuators A: Phys. 123/124 (2005) 497–504.
[10] C.R. Buie, J.D. Posner, T. Fabian, C.A. Suk-Won, D. Kim, F.B. Prinz, J.K. Eaton, J.G. Santiago, J. Power Sources 161 (1) (2006) 191–202.
[11] H.A. Gasteiger, S.S. Kocha, B. Sompalli, F.T. Wagner, Appl. Catal. B: Environ. 56 (1/2) (2005) 9–35.
[12] J.R. Yu, B.L. Yi, D.M. Xing, F.Q. Liu, Z.G. Shao, Y.Z. Fu, Phys. Chem. Chem. Phys. 5 (3) (2003) 611–615.
[13] A. Collier, H.J. Wang, X.Z. Yuan, J.J. Zhang, D.P. Wilkinson, Int. J. Hydrogen Energy 31 (13) (2006) 1838–1854.
[14] H.L. Tang, P.K. Shen, S.P. Jiang, W. Fang, P. Mu, J. Power Sources 170 (1) (2007) 85–92.
[15] J.R. Yu, T. Matsuura, Y. Yoshikawa, M.N. Islam, M. Hori, Phys. Chem. Chem. Phys. 7 (2) (2005) 373–378.
[16] D.A. Schiraldi, Polym. Rev. 46 (3) (2006) 315–327.
[17] X. Cheng, J.L. Zhang, Y.H. Tang, C.J. Song, J. Shen, D.T. Song, J.J. Zhang, J. Power Sources 167 (1) (2007) 25–31.
[18] K.J. Jeong, C.A. Miesse, J.H. Choi, J. Lee, J. Han, S.P. Yoon, S.W. Nam, T.H. Lim, T.G. Lee, J. Power Sources 168 (1) (2007) 119–125.
[19] E. Kjeang, J. Goldak, M.R. Golriz, J. Gu, D. James, K. Kordesch, Fuel Cells 5 (4) (2005) 486–498.
[20] S.S. Kocha, J.D.L. Yang, J.S. Yi, AIChE J. 52 (5) (2006) 1916–1925.
[21] B.H. Liu, S. Suda, J. Power Sources 164 (1) (2007) 100–104.
[22] M.K. Ravikumar, A.K. Shukla, J. Electrochem. Soc. 143 (8) (1996) 2601–2606.
[23] E.R. Choban, L.J. Markoski, A. Wieckowski, P.J.A. Kenis, J. Power Sources 128 (1) (2004) 54–60.
[24] R.S. Jayashree, L. Gancs, E.R. Choban, A. Primak, D. Natarajan, L.J. Markoski, P.J.A. Kenis, J. Am. Chem. Soc. 127 (48) (2005) 16758–16759.
[25] G.H. Miley, N. Luo, J. Mather, R. Burton, G. Hawkins, L.F. Gu, E. Byrd, R. Gimlin, P.J. Shrestha, G. Benavides, J. Laystrom, D. Carroll, J. Power Sources 165 (2) (2007) 509–516.
[26] R. Ferrigno, A.D. Stroock, T.D. Clark, M. Mayer, G.M. Whitesides, J. Am. Chem. Soc. 124 (44) (2002) 12930–12931.
[27] E. Kjeang, J. McKechnie, D. Sinton, N. Djilali, J. Power Sources 168 (2) (2007) 379–390.
[28] R.S. Jayashree, M. Mitchell, D. Natarajan, L.J. Markoski, P.J.A. Kenis, Langmuir 23 (13) (2007) 6871–6874.
[29] J.L. Cohen, D.A. Westly, A. Pechenik, H.D. Abruna, J. Power Sources 139 (1/2) (2005) 96–105.
[30] M.H. Sun, G.V. Casquillas, S.S. Guo, J. Shi, H. Ji, Q. Ouyang, Y. Chen, Microelectron. Eng. 84 (5–8) (2007) 1182–1185.
[31] R.F. Probstein, Physicochemical Hydrodynamics: An Introduction, 2nd ed., Wiley, 2003.
[32] J.G. Santiago, S.T. Wereley, C.D. Meinhart, D.J. Beebe, R.J. Adrian, Exp. Fluids 25 (4) (1998) 316–319.
[33] David R. Lide (Ed.), CRC Handbook of Chemistry and Physics, 87th ed. (Internet Version 2007), CRC Press/Taylor and Francis, Boca Raton, FL.
[34] F.A. Cotton, G. Wilkinson, Advanced Inorganic Chemistry, 4th ed., John Wiley & Sons, 1980.
[35] F.M. White, Viscous Fluid Flow, McGraw Hill, 2006.
[36] J.S. Bendat, A.G. Piersol, Random Data: Analysis & Measurement Procedures, John Wiley & Sons, 2000.
[37] J. Larminie, A. Dicks, Fuel Cell Systems Explained, 2nd ed., John Wiley & Sons, San Francisco, CA, 2003, p. 406.
[38] T. Lis, B. Jezowskatrzebiatowska, Acta Crystallogr. Sect. B: Struct. Sci. 33 (July 15) (1977) 2112–2116.
[39] A. Bazylak, D. Sinton, N. Djilali, J. Power Sources 143 (1/2) (2005) 57–66.
[40] M.H. Chang, F. Chen, N.S. Fang, J. Power Sources 159 (2) (2006) 810–816.
[41] F.L. Chen, M.H. Chang, M.K. Lin, Electrochim. Acta 52 (7) (2007) 2506–2514.